Journal of Nanobiotechnology

RESEARCH

Open Access

Mitochondria-targeting polymer cLipG/CuET activates the cGAS/STING pathway to enhance cholangiocarcinoma immunotherapy

Ge Bai[1†], Hongwen Liu[2†], Wei Li[2†], Sijia Chen[2†], Lishan Wang[1], Zhangding Wang[2], Yue Zhou[2], Yani Pan[2], Yu Liu[2], Qi Chen[3], Nannan Zhang[3], Jingjing Wei[1], Xueni Fu[1], Yaru Zhou[3], Yun Zhu[2,4*], Lei Xu[2*] and Lei Wang[1,2*]

Abstract

Background The remodeling of extracellular matrix often fails chemotherapeutic agents to fight intrahepatic cholangiocarcinoma (ICC). The cGAS/STING pathway can trigger the innate immune response to obtain better immunotherapeutic outcomes.

Results A cLipG/CuET nanocomposite was designed and synthesized based on glycyrrhizic acid (GA) and copper diethyldithiocarbamate (CuET). GA can open mitochondrial permeability transition pores (MPTPs), allowing Cu (II) to interrupt mitochondrial function through copper toxicity. By activating the cGAS-STING signaling pathway in macrophages, this mitochondrial-targeting polymer (cLipG/CuET) significantly boosted the production of mitochondrial reactive oxygen species (mtROS), and promoted the escape of damaged mitochondrial DNA (mtDNA) from ICC cells. Consequently, M1 polarization of cancer-associated macrophages enhanced the immune response against ICC. In the mouse model, the intravenous administration of cLipG/CuET transformed the ICC from "cold" into "hot".

Conclusions With a high biosafety, cLipG/CuET exerted a synergistic effect on the immune checkpoint inhibitor αCTLA-4 against ICC, and their combination provided a new therapeutic strategy.

Keywords Cholangiocarcinoma, Nanoliposomes, Cuproptosis, Mitochondria, Immune-sensitizing therapy

†Ge Bai, Hongwen Liu, Wei Li and Sijia Chen contributed equally to this work.

*Correspondence:
Yun Zhu
zjuzhuyun@163.com
Lei Xu
dr_leixu@163.com
Lei Wang
leiwang9631@nju.edu.cn

Full list of author information is available at the end of the article

Graphical abstract

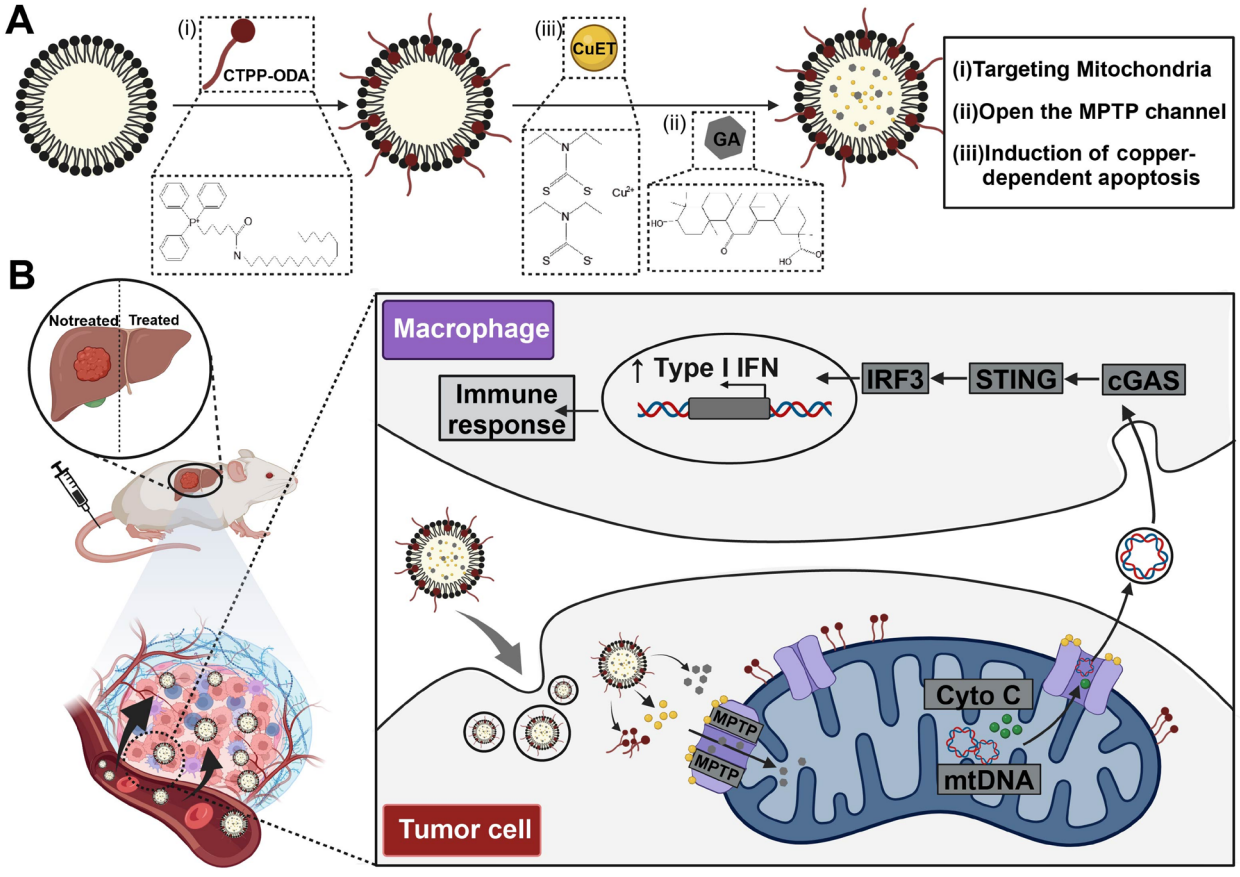

Background

Intrahepatic cholangiocarcinoma (ICC) is a rare but highly invasive malignancy, with a poor prognosis and an incidence ever-increasing annually [1, 2]. ICC is structurally characterized by a fibrogenic extracellular matrix and a hypovascular stroma, containing a mixture of non-immune and immune cells, such as cancer-associated fibroblasts and tumor-associated macrophages [3]. This structure does not favor therapeutic agents to exhaust their therapeutic potentials. Studies have shown that CTLA-4-positive lymphocytes are more enriched in ICC tissues than in peritumoral liver tissues. The activation of PD-1/PD-L1 and CTLA-4 signals is correlated with a poor prognosis of ICC, suggesting a therapeutic potential in CTLA-4-targeting agents. CTLA-4 blockade protects against cancers by initiating anti-tumor immunity and expanding the pool of infiltrating $CD8^+$ T cells [4]. Currently, surgical resection is recommended as the mainstay treatment for early-stage ICC, and gemcitabine combined with cisplatin for unresectable or metastatic ICC. Alternative strategies, such as locoregional therapy, targeted therapy, and immunotherapy [5], have also shown their pros and cons. Nevertheless, more effective treatment arsenals need to be developed to improve the prognosis of ICC patients.

The cGAS (cyclic GMP-AMP synthase)/STING (stimulator of interferon genes) signaling pathway, for its crucial role in the immunomodulation of cancer cells, has garnered researchers' attention [6]. After tumor-derived double-stranded DNA (dsDNA) leaks into the cytoplasm, its accumulation hijacks the cytosolic DNA sensor cGAS to catalyze the synthesis of cyclic GMP-AMP (cGAMP) and thus activates the adaptor protein STING [7]. Moreover, a series of mitochondrial dysfunction events, such as loss of apoptotic caspases, defects in mitochondrial DNA (mtDNA) condensation, and impairment in mitophagy, can also trigger the activation of the cGAS/STING signaling pathway [8]. The release of damaged mtDNA is broadly involved in the initiation of cGAS responses in various diseases, like COVID-19 and amyotrophic lateral sclerosis (ALS) [9, 10]. STING first induces the production of type I interferons (IFN-I), which in turn enhances antigen presentation and activates $CD8^+$ cytotoxic T lymphocytes (CTLs) to combat cancer cells [11]. Then, the interplay between cancer cells and immune cells further drives the release of immunogenic factors (e.g., mtDNA)

from tumor cells, thereby activating the cGAS/STING signaling pathway in antigen-presenting cells to enhance the host's immune response [12].

Cuproptosis is a newly discovered form of regulated cell death uniquely associated with copper-induced mitochondrial dysfunction. An intracellular accumulation of copper evokes the aggregation of mitochondrial lipoylated proteins and destabilization of Fe-S cluster proteins, providing a new clue to design mitochondria-targeted therapies against ICC [13]. However, anti-cancer properties of copper ions rely on a maintenance of copper homeostasis and an interaction with other proteins. For instance, the copper chaperone for superoxide dismutase (CCS) can transfer copper ions to the enzymes by directly interacting with superoxide dismutase 1 (SOD1) that plays a critical role in maintaining the intracellular homeostasis of reactive oxygen species (ROS) [14]. However, copper ions are difficult to be introduced into mitochondria, thus necessitating the design of precise drug delivery systems.

The mitochondrial permeability transition pore (MPTP), a significant channel in the inner mitochondrial membrane, opens under conditions of high matrix Ca^{2+} and oxidative stress [15]. Frequent and persistent MPTP opening can increase ROS production, electron leakage, and decrease mitochondrial membrane potential (MMP), thus promoting cell apoptosis [16]. 18β-Glycyrrhetinic acid (GA), an active component derived from the traditional Chinese medicine (TCM) herbal Licorice (*Glycyrrhiza uralensis*) [17], can cause mitochondrial damages by opening the MPTP [18]. GA induces oxidative stress by interacting with the Fe-S clusters in mitochondrial Complex I of the electron transport chain. This interaction leads to the generation of hydrogen peroxide (H_2O_2) [19], which subsequently oxidizes critical thiol groups and endogenous pyridine nucleotides. These oxidative modifications ultimately trigger the opening of the MPTP [20]. Therefore, we propose that GA in conjunction with other drugs can enhance the efficiency of drug delivery by opening MPTP.

In the present study, a novel drug delivery system was designed and synthesized utilizing phospholipids as nanocarriers to activate the cGAS/STING signaling pathway within cancer cells. First, a hydrophobic lipophilic compound (CTPP-ODA) was synthesized by conjugating (4-carboxybutyl) triphenylphosphonium bromide (CTPP) with octadecylamine (ODA) under the catalysis of catalyst. CTPP, as a cation with sufficient lipophilicity and delocalized positive charge, allows an effective accumulation in mitochondria by reducing the free energy change responsible for the transfer from an aqueous to a hydrophobic environment [21], thus increasing the efficiency of transmembrane transport and targeting in tumor cells with high membrane potential [22, 23]. Third, the cLipo was modified with disulfiram copper (CuET) to form nanoparticles (Lipo@CuET, cLipo/CuET) with a stronger anti-cancer efficacy.

CuET is a novel copper ethylthiocarbamate complex formed by the drug disulfiram (DSF), primarily used for treating alcohol addiction in combination with copper [24]. Due to the presence of copper, CuET greatly enhances the anti-cancer property of DSF. However, CuET has a poor solubility and a limited permeability. To overcome these drawbacks, we finally synthesized nanoparticles (Lipo-GA@CTPP-ODA@CuET, cLipG/CuET) by encapsulating GA into cLipo. Overall, the cLipG/CuET exerted potent anti-cancer properties, in which GA targeted to open the MPTP and promoted mitochondrial delivery of CuET, and CuET further undertook the duty of killing tumor cells. Notably, delivered Cu^{2+} can effectively induce copper-dependent mitochondrial damage and mediate the release of damaged mitochondrial DNA fragments, eventually activating the cGAS/STING signaling pathway to initiate innate immunity. The cLipG/CuET also assisted in the efficacy of immune checkpoint inhibitors by reprograming tumor-associated macrophages (TAMs). In summary, the cLipG/CuET nanoparticles may bring new benefits to ICC patients by improving cancer immunogenicity.

Results

Preparation and characterization of the cLipG/CuET

The triphenylphosphonium cation ($CTPP^+$) is the most widely used mitochondrial- targeting carrier, owing to its high targeting efficiency and relative stability in biological systems [25]. Catalyzed by N-hydroxysuccinimide (NHS) and 1-ethyl-3-(3-dimethylaminopropyl) carbodiimide (EDC), CTPP was conjugated with ODA to synthesize a hydrophobic-lipophilic compound CTPP-ODA (Fig. 1A). In the CTPP-ODA spectrum, the characteristic peak of the -CH3 group of ODA was observed at approximately 1.3 ppm, and the distinctive peak of CTPP was shifted to around 7.3 ppm (Fig. 1B), suggesting a successful synthesis of CTPP-ODA.

CTPP-ODA was used to modify liposomes and encapsulate GA, followed by a further modification with the CuET (cLipG/CuET). CTPP-modified GA or CuET liposomes (controls) were compared with cLipG/CuET (Fig. 1C). Transmission electron microscopy (TEM) images confirmed the nanoscale structure of the liposomes, showing uniform spherical shapes and deep dispersion (Fig. 1D). Additionally, TEM-EDS elemental mapping analysis verified the existence of Cu in the cLipG/CuET composite (Fig. 1E). Dynamic light scattering (DLS) measurements further indicated an average diameter of 105.7 nm for cLipG, 110.17 nm for cLipo/CuET, and 123.05 nm for cLipG/CuET (Fig. 1F). The Zeta potentials of cLipG, cLipo/CuET, and cLipG/CuET were

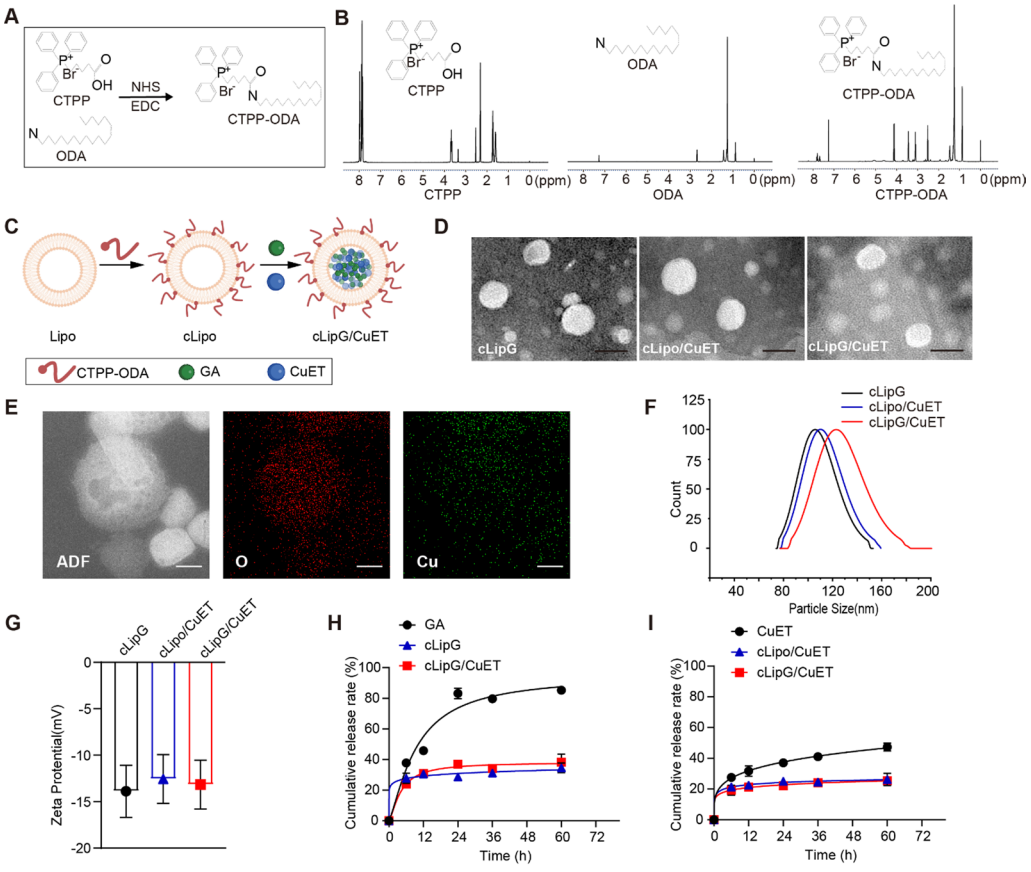

Fig. 1 Preparation and Characterization of the cLipG/CuET. **A** Synthesis of CTPP-ODA. **B** ^{1}H-NMR analysis of CTPP, ODA and CTPP-ODA. **C** The scheme of cLipG/CuET synthesis. **D** Morphological characteristics of cLipG, cLipo/CuET, and cLipG/CuET examined by TEM, scale bar = 50 μm. E The elemental distribution map of cLipG/CuET examined by TEM-EDS, scale bar = 50 μm. **F** DLS measurements of the cLipG, cLipo/CuET, and cLipG/CuET in water. **G** Zeta potential measurements of surface charge of cLipG, cLipo/CuET, and cLipG/CuET in the water. **H**, **I** Evaluation of cumulative drug release rates from the carriers at pH 7.4

measured at −10.17 ± 2.455 mV, −8.50 ± 3.018 mV, and −8.12 ± 3.018 mV, respectively (Fig. 1G).

We measured the kinetics in the release of phosphate buffer saline (PBS) at a neutral pH, and plotted drug release curves. Cumulative amounts of GA and CuET released from cLipG/CuET were measured at predetermined intervals, and compared with those in the free and single-loaded groups. A slower drug release was observed in both the single-loaded and dual-loaded groups, compared to the free group, although it was comparable between the former two groups (Fig. 1H and I). Collectively, the cLipG/CuET nanoparticles were small in size, and possessed negative charges. Additionally, their ability to slow down payload release in neutral solutions suggested a prolonged circulation time.

Cellular uptake and mitochondria-targeting effect of cLipG

To investigate the cellular uptake and intracellular release of modified liposomes in tumor cells, the cholangiocarcinoma cell line HuCCT1 was incubated with the cLipG loaded with Coumarin 6 (green fluorescence) (cLipG/C6) for 6 h. Under the fluorescence microscope, cLipG/C6 exhibited the strongest fluorescence signal in HuCCT1 cells than the Lipo/C6 and cLipo/C6 (Fig. 2A, B). Fluorescence was barely seen in the free C6 group. The fluorescence was significantly more evident in the Lipo/C6 and cLipo/C6 groups than in the free C6 group, and the most pronounced in the cLipG/C6. Flow cytometry data also confirmed that CTPP and GA modifications in the liposomes significantly elevated cellular uptake (Fig. S1A, Fig. 2C).

To validate the mitochondrial delivery of the fluorescent probe (C6) as a substitute for CuET, we isolated mitochondria from HuCCT1 cells and performed flow cytometry. The efficiency of mitochondrial isolation was confirmed by Western blot analysis using TOM20 as a mitochondrial marker (Fig. S1C). Flow cytometric results demonstrated a significantly higher fluorescence intensity in the mitochondria of cLipG/C6-treated tumor cells (Fig. S1B, Fig. 2D), confirming the high efficiency of cLipG-mediated mitochondrial delivery.

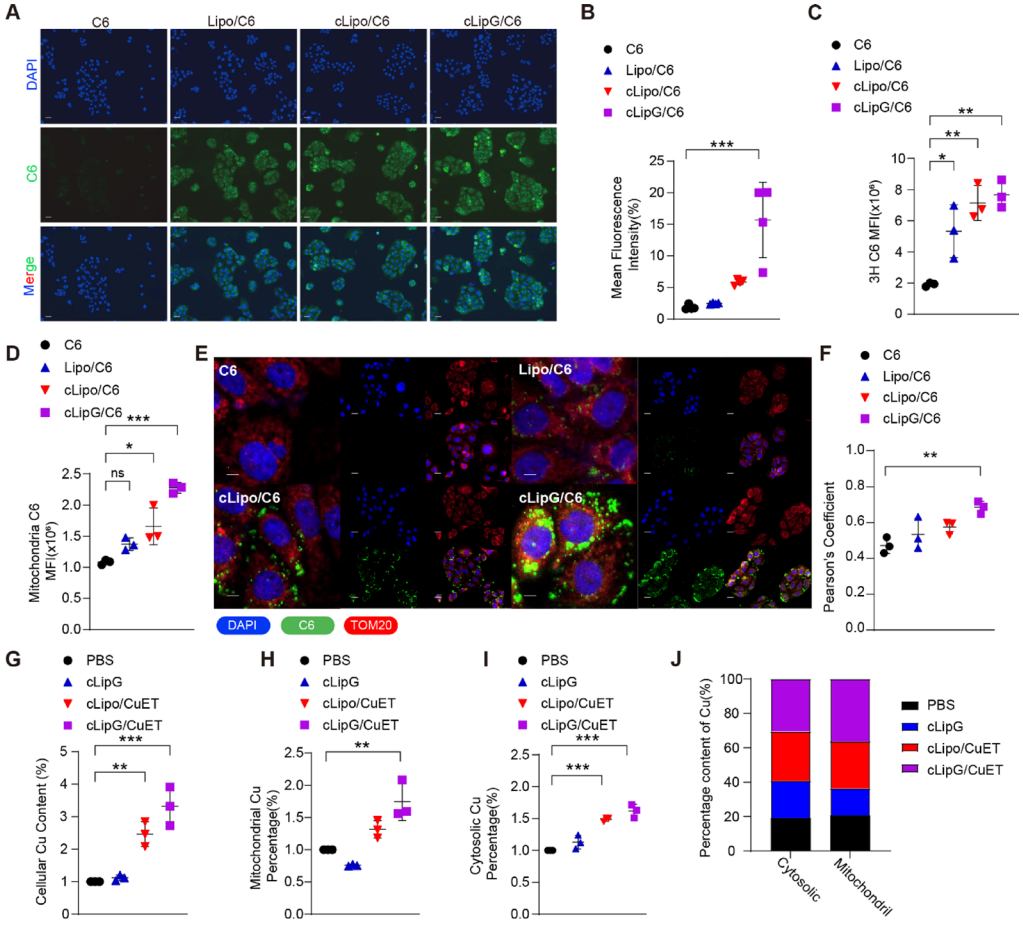

Fig. 2 Cellular Uptake and Mitochondrial-Targeting Effect of cLipG. **A** Cellular uptake of C6 in the free C6, Lipo/C6, cLipo/C6, and cLipG/C6 by HuCCT1 cells shown by confocal microscopy, scale bar = 50 μm. **B** A semi-quantitative analysis of the fluorescence intensity of C6. **C** Flow cytometry of cellular uptake of free C6, Lipo/C6, cLipo/C6, and cLipG/C6 by HuCCT1 cells. **D** Flow cytometry of the uptake of free C6, Lipo/C6, cLipo/C6, and cLipG/C6 in HuCCT1 cell mitochondria. **E** Fluorescence staining of C6 (green) and TOM20 (red) in free C6, Lipo/C6, cLipo/C6, and cLipG/C6 by HuCCT1 cells, scale bar = 50 μm. **F** Quantitative analysis of the Pearson's correlation coefficient for the colocalization of lipid carriers and mitochondria. **G** The relative contents of Cu^{2+} in HuCCT1 cells incubated with PBS, cLipG, cLipo/CuET, and cLipG/CuET, respectively. **H** The relative contents of Cu^{2+} in mitochondria incubated with PBS, cLipG, cLipo/CuET, and cLipG/CuET, respectively. **I** The relative contents of Cu^{2+} in cytoplasm incubated with PBS, cLipG, cLipo/CuET, and cLipG/CuET, respectively. **J** The Cu^{2+} ratio between mitochondria and cytoplasm. One-way ANOVA was conducted (SD, $n = 3$). $^{*}P < 0.05$, $^{**}P < 0.01$, $^{***}P < 0.001$

The specific targeting ability of cLipG in mitochondria was then explored. Besides the significantly stronger green signal in the cLipG/C6 group, the overlap with the mitochondrial marker TOM20 (red) was also more pronounced than that in other groups (Fig. 2E). Then, Pearson's correlation coefficient of the cLipG/C6 was closer to 1, indicating a colocalization in the mitochondria [26, 27] (Fig. 2F). To further verify the role of cLipG in delivering CuET into cells and even mitochondria, we quantitatively measured Cu^{2+} concentrations in whole cells, mitochondrial fractions, and cytoplasmic compartments. (Fig. 2G, H, I). Cu^{2+} levels increased in both whole cells and subcellular fractions, with the most pronounced accumulation in the cLipG/CuET treatment group. Notably, mitochondrial Cu^{2+} content was substantially higher than that in the cytoplasmic compartment (Fig. 2J). Taken together, cLipG/CuET had a strong ability to increase cellular uptake and target mitochondria.

Cytotoxicity and cell apoptosis analysis of cLipG/CuET

We initially evaluated the cytotoxicity of free GA and CuET in HuCCT1 cholangiocarcinoma cells using the CCK8 assay (Fig. S1D, Fig. 3A), which revealed a low cytotoxicity of free CuET on HuCCT1 cells, possibly due to its poor cellular and mitochondria uptake. Liposomes and CTPP-ODA significantly enhanced the in vitro antitumor efficacy of CuET. Their combination, especially cLipG/CuET with GA@CTPP in a ratio of 2:4, exhibited a significantly stronger anti-tumor effect on HuCCT1 cells than cLipo/CuET and cLipG alone (Fig. 3A).

The Zero interaction potency (ZIP) model was created to capture the dose-response curves of cLipG combined with cLipo/CuET (Fig. 3B). Generally, synergy scores

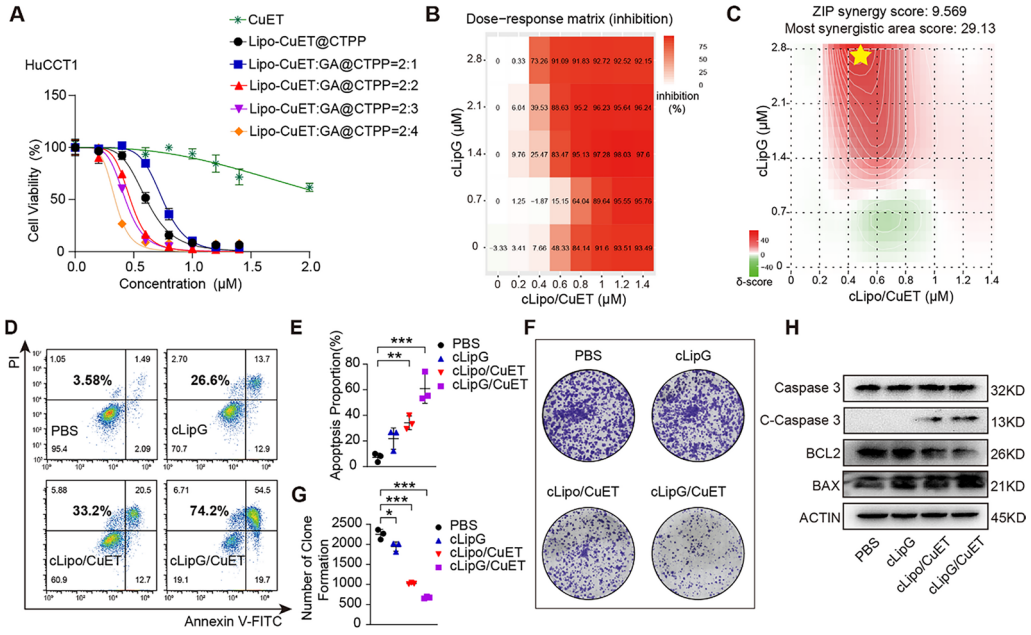

Fig. 3 Cytotoxicity of the cLipG/CuET and its Pro-apoptotic Ability in ICC. **A** CCK-8 assay of the cytotoxicity of cLipo/CuET and cLipG/CuET against HuCCT1 cells. **B** Dose-response matrices of cLipG combined with cLipo/CuET. **C** A heatmap visualizing the combination responses of cLipG and cLipo/CuET, and corresponding synergy scores. **D** Annexin V/PI staining combined with flow cytometry of cell apoptosis. **E** A semi-quantitative analysis of cell apoptosis. **F** Representative images of the colony formation assay. **G** A semi-quantitative analysis of colony formation rates. **H** Protein expressions of Caspase 3, cleaved Caspase 3 (C-Caspase 3), BCL_2, and BAX in HuCCT1 cells. One-way ANOVA was conducted (SD, $n = 3$). $^*P < 0.05$, $^{**}P < 0.01$, and $^{***}P < 0.001$

below − 10, between − 10 and 10, and above 10 indicate antagonism, additivity, and synergy, respectively [28, 29]. The synergy map of cLipG and cLipo/CuET showed that in HuCCT1 cells, the mean (and maximum) combination index for the anti-tumor response due to drug interactions was 9.569 (29.13). The synergy plot of cLipG and cLipo/CuET revealed that the mean (and maximum) combination index for drug interaction-induced antitumor response in HuCCT1 cells was 9.569 (29.13). This indicated an overall additive effect (−10 < ZIP synergy score < 10) between cLipo/CuET and cLipG in suppressing tumor proliferation. The combination of 2.8 μM cLipG and 0.5 μM cLipo/CuET demonstrated remarkable synergistic effects, with a combination index (CI) of 29.13. Therefore, this concentration ratio with a pentagram (★) in the figure was adopted in the following experiments (Fig. 3C).

To further investigate the impact of cLipG/CuET on the apoptosis of HuCCT1 cells, Annexin V/PI analysis staining combined with flow cytometry was performed. Compared to the control group, inductions with cLipG and cLipo/CuET showed limited pro-apoptotic effects on HuCCT1 cells, whereas the cLipG/CuET treatment significantly stimulated the apoptosis in 74.2% of HuCCT1 cells (Fig. 3D, E). Colony formation assay revealed a significantly decreased colony formation rate in HuCCT1 cells induced with cLipo/CuET and cLipG/CuET by 50% and 70%, respectively (Fig. 3F, G). Additionally, the pro-apoptotic proteins Cleaved-Caspase3 and BAX were significantly upregulated, while the anti-apoptotic protein BCL_2 was significantly downregulated in HuCCT1 cells induced with cLipG/CuET (Fig. 3H). These results suggested that cLipG/CuET exerted a promising therapeutic effect against ICC by activating apoptosis and inhibiting colony formation.

cLipG/CuET mediated opening of the MPTP

Considering the mitochondria-targeting and pro-apoptotic properties of cLipG/CuET, as well as the role of GA in promoting the opening of the MPTP [18], we hypothesized that MPTP facilitates the entry of cLipG/CuET into mitochondria via CTPP attachment on the mitochondrial surface, thereby inducing mitochondrial changes and apoptosis in cancer cells. To evaluate the impact of cLipG/CuET on MPTP opening, the cells were loaded with the fluorescent probe Calcein that distributes throughout the cytosol and mitochondria, and treated with $CoCl_2$ to quench the fluorescence of Calcein. Once the MPTP opened, $CoCl_2$ entered the mitochondria to extinguish the fluorescence signal of Calcein (Fig. 4A). Here, the treatment with cLipG/CuET resulted in a significant reduction in Calcein fluorescence, indicating the ability of cLipG/CuET in triggering the opening of MPTP (Fig. 4B, C).

Downregulation of ferredoxin-1 (FDX1) and dihydrolipoamide S-acetyltransferase (DLAT), and lipoic acid synthase (LIAS) confirmed the role of cLipG/CuET in disrupting mitochondrial energy metabolism

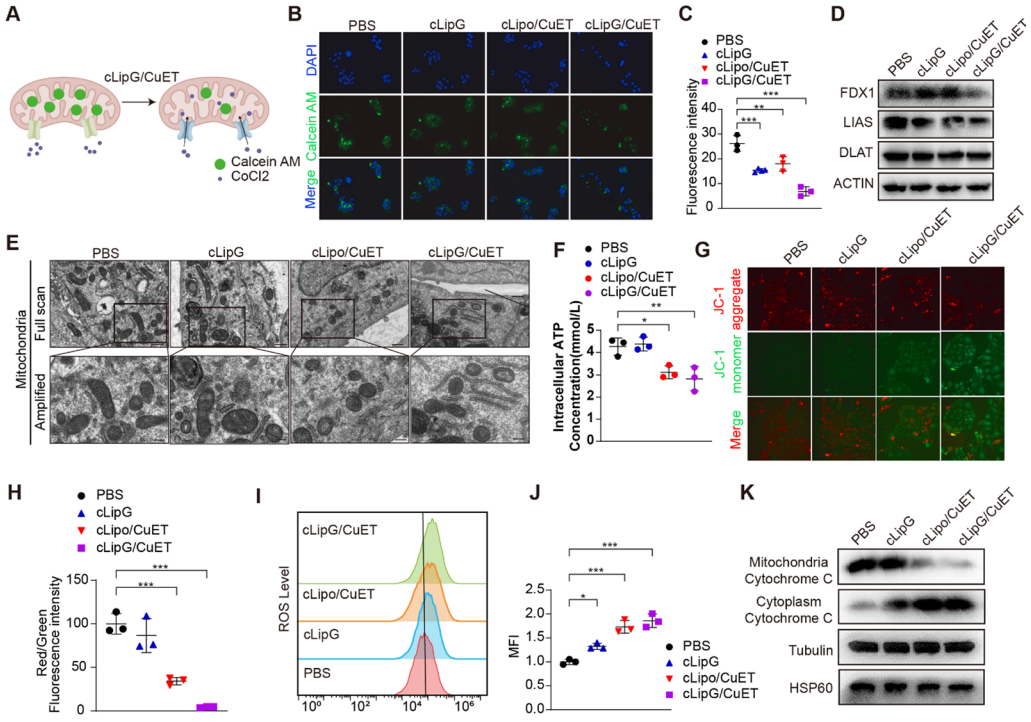

Fig. 4 cLipG/CuET Targets Mitochondria and Facilitates MPTP opening. **A** A scheme of MPTP opening induced by cLipG/CuET. **B** Representative fluorescence images of Calcein-AM staining in HuCCT1 cells induced with PBS, cLipG, cLipo/CuET, and cLipG/CuET, respectively, scale bar = 50 μm. **C** A semi-quantitative analysis of fluorescence intensity of Calcein-AM **D** Western blotting of copper-dependent cell death-related proteins FDX1, LIAS, and DLAT. **E** Bio-TEM images visualizing mitochondrial morphology in HuCCT1 cells induced with PBS, cLipG, cLipo/CuET, and cLipG/CuET, respectively, scale bars = 500 nm and 250 nm. **F** Detection of intracellular ATP levels by ELISA. **G** Fluorescence images of HuCCT1 cells stained with JC-1, scale bar = 50 μm. **H** A semi-quantitative analysis of fluorescence intensity of red/green JC-1. **I** Intracellular ROS levels in HuCCT1 cells induced with PBS, cLipG, cLipo/CuET, and cLipG/CuET using the DCFH-DA probe, respectively. **J** Quantitative analysis of intracellular ROS levels. **K** Western blotting of a mitochondrial and cytoplasmic cytochrome C in HuCCT1 cells induced with PBS, cLipG, cLipo/CuET, and cLipG/CuET, respectively. One-way ANOVA was conducted (SD, $n = 3$). $^{*}P < 0.05$, $^{**}P < 0.01$, and $^{***}P < 0.001$

to effectively induce copper-dependent cell death (Fig. 4D). TEM visualized severe mitochondrial damage after a cellular uptake of cLipG/CuET, characterized by mitochondrial shrinkage, membrane high-density, and the reduction or disappearance of mitochondrial cristae (Fig. 4E). Consequently, the intracellular ATP level, generated via mitochondrial activity, also significantly decreased (Fig. 4F). JC-1 staining showed that cLipG/CuET-induced HuCCT1 cells exhibited a larger loss of mitochondrial membrane potential (Δψ) than other groups (Fig. 4G, H).

The increased copper content in tumor cells leads to a significant depletion of glutathione (GSH), arousing Fenton-like reactions to produce a large amount of ROS [30]. Eventually, accumulated ROS further induces oxidative stress and mitochondrial damage. In our study, the intracellular ROS level was significantly higher in cLipG/CuET-induced HuCCT1 cells than in other groups (Fig. 4I, J). Cytochrome C is an integral component of the mitochondrial respiratory chain and typically tightly bound to the inner mitochondrial membrane [31]. The opening of MPTP, or the hyperpermeability of the outer mitochondrial membrane, results in the release of cytochrome C from the mitochondria into the cytosol [32]. A decrease in mitochondrial cytochrome C and an increase in cytosolic cytochrome C following the treatment with cLipG/CuET further indicated the opening of the MPTP (Fig. 4K).

cLipG/CuET enhances the immune response in vitro

Mitochondrial damage and mtDNA release following MPTP channel opening can directly activate the cGAS-STING pathway to enhance the immune response [10]. We purified DNA from cytosolic extracts of HuCCT1 cells for qPCR analysis and found enriched mtDNA in the cytosol of cLipG/CuET-treated tumor cells (Fig. 5A). Immunofluorescence imaging showed a significant reduction in the overlap of the red fluorescence from mitochondrial transcription factor A (TFAM)-bound mtDNA with the green fluorescence from the mitochondrial marker mitochondrial translocation enzyme 20 (TOM20) (Fig. 5B), indicating an increased release of mtDNA from mitochondria.

To elucidate the immunostimulatory effect of cLipG/CuET on immune cells, the macrophage cell line THP-1 was co-cultured with the supernatant of cLipG/

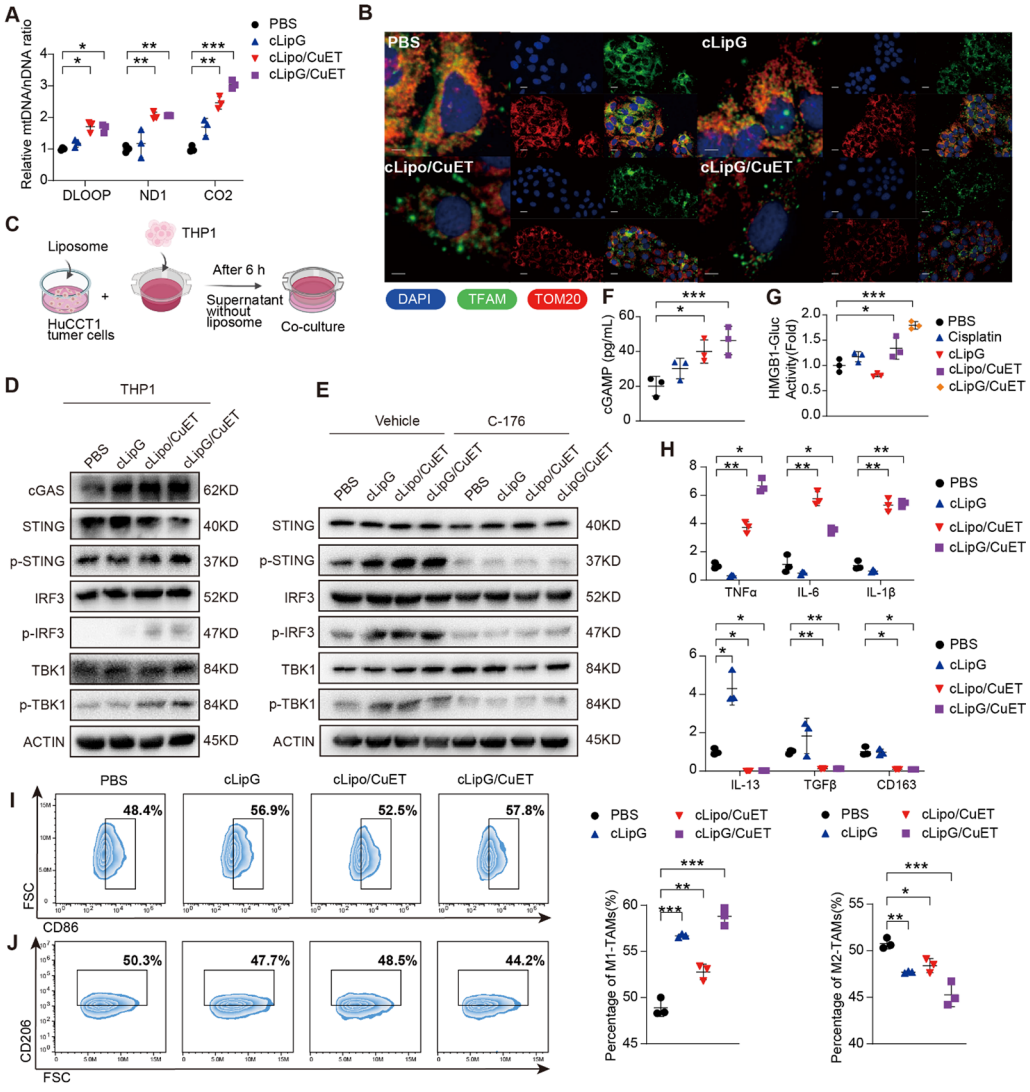

Fig. 5 cLipG/CuET Activates the Immune Response Against ICC In Vitro. **A** qPCR analysis of mtDNA in cytoplasmic extracts of HuCCT1 cells induced with PBS, cLipG, cLipo/CuET, and cLipG/CuET, respectively. **B** Immunofluorescence staining of TOM20 (red), TFAM (green), and DAPI (blue) in HuCCT1 cells induced with PBS, cLipG, cLipo/CuET, and cLipG/CuET, repectively; scale bar = 25 μm. **C** A scheme of the Transwell co-culture system of THP-1 cells with the supernatant from of HuCCT1 cells induced with PBS, cLipG, cLipo/CuET, and cLipG/CuET, respectively. **D** Western blotting assessed the expression levels of cGAS, STING, p-STING, IRF3, p-IRF3, TBK1, and p-TBK1 in THP1. **E** Western blotting assessed the expression levels of STING, p-STING, IRF3, p-IRF3, TBK1, and p-TBK1 in THP1 treated with either vehicle or C-176. **F** Measurement of cGAMP release levels from HuCCT1 cells using ELISA. **G** Detection of HMGB1 levels in the supernatants from of HuCCT1 cells induced with PBS, cisplatin, cLipG, cLipo/CuET, and cLipG/CuET. **H** Differentiation levels of THP1 cells polarized into M1 and M2 macrophages after co-culture with the supernatant of HuCCT1 cells induced with PBS, cisplatin, cLipG, cLipo/CuET, and cLipG/CuET. **I**, **J** Proportions of M1-TAMs ($F4/80^+CD86^+$) and M2-TAMs ($F4/80^+CD206^+$). One-way ANOVA was conducted (SD, $n = 3$). $^*P < 0.05$, $^{**}P < 0.01$, and $^{***}P < 0.001$

CuET-treated HUCCT1 cells in a Transwell co-culture system (Fig. 5C). Interestingly, the mtDNA from cLipG/CuET-treated HUCCT1 cells was transferred to macrophages in the TME, thereafter activating cGAS to synthesize cGAMP (Fig. 5F). Protein expressions of key molecules associated with the cGAS/STING pathway in macrophages were detected by Western blotting. Compared to other groups, the cLipG/CuET group showed higher phosphorylation levels of STING, IRF3, and TBK1 (Fig. 5D). Furthermore, treatment with the STING inhibitor C-176 significantly reduced the phosphorylation levels of key pathway components (Fig. 5E), suggesting that mitochondrial damage triggered by cLipG/CuET promoted the activation of the cGAS-STING pathway.

Additionally, we detected the release of high mobility group protein 1 (HMGB1) using a luciferase reporter assay. Treatment with cLipG/CuET increased HMGB1 production in the cell supernatant (Fig. 5G). Based on our findings that cLipG/CuET activates the cGAS/STING pathway in macrophages, we hypothesized that

these liposomes may promote the polarization of tumor-associated macrophages (TAMs) preferably towards the M1 phenotype. After an incubation with the supernatant of cLipG/CuET-pretreated HuCCT1 cells, a significant upregulation of M1 markers and a downregulation of M2 markers were observed in macrophages (Fig. 5H). Flow cytometry consistently showed a higher proportion of M1 macrophages and a lower of M2 macrophages in the cLipG/CuET group, compared to other groups (Fig. 5I, J).

Taken together, cLipG/CuET repolarized TAMs towards the M1 phenotype by activating the cGAS/STING signaling pathway, thus enhancing the immune response in ICC in vitro.

In vivo distribution of cLipG

In vivo pharmacokinetics of cLipG/CuET was examined in a KRAS^{G12D}/P19 plasmid-induced primary cholangiocarcinoma (CCA) mouse model, where cLipG was labeled with IR780 instead of CuET. IR780 is a near-infrared fluorescent dye with an emission wavelength in the near-infrared region (around 830 nm) [33]. IR780 labelling avoided the interference of autofluorescence from other substances within biological tissues, thereby achieving clearer and more accurate imaging results in mouse models.

An in vivo imaging system was used to analyze the biodistribution of free IR780 solution, Lipo/IR780, cLipo/IR780, and cLipG/IR780 in CCA mice at post-tail-injection 1, 4, 8, and 24 h (Fig. 6A). Accumulation of cLipG/IR780 at the tumor site started at 1 h and peaked at 8 h. In contrast, accumulations of free IR780, Lipo/IR780, and cLipo/IR780 declined after 24 h (Fig. 6B, C). This indicated that cLipG prolonged the retention of the payload at the tumor site and reduced drug release rate. Tumor-bearing mouse livers exhibited the most intense fluorescence (Fig. 6D, E), indicating that cLipG demonstrated an excellent tumor-targeting ability in vivo. To verify the targeted delivery of fluorescent probes to hepatic tumor sites, we performed in vivo fluorescence tracking studies using C6-loaded liposomal formulations (including cLipG/C6) administered intravenously via tail vein injection in an orthotopic liver tumor mouse model. Confocal laser scanning microscopy demonstrated specific accumulation of green signals in tumor-bearing liver tissues (Fig. 6F), showing a statistically significant enhancement in fluorescence intensity ($p < 0.001$) for the cLipG/C6 formulation compared to control groups (Fig. 6G), thereby confirming the effective tumor-targeting capability of the cLipG delivery system.

Synergistic effects of cLipG/CuET and αCTLA-4 against ICC in vivo

Recent studies have shown that the activated STING signaling pathway accounts for the anti-tumor effects of immune checkpoint blockades (ICBs) [34], including antibodies against PD-L1, PD-1, and CTLA-4. Consequently, anti-tumor immunotherapy can be considered a vehicle for driving innate immunity [35]. Given the role of cLipG/CuET in enhancing the immune response in vitro, we hypothesized that cLipG/CuET in combination with CTLA-4 blockade (αCTLA-4) could provide a synergistic effect on ICC. An orthotopic CCA model was created by injecting the KRAS ^{G12D}/P19 plasmid via the tail vein at 14 days prior to the first intravenous injection of cLipG/CuET (day − 14). Mice were then randomly divided into four groups: PBS, cLipG/CuET, αCTLA-4, and cLipG/CuET + αCTLA-4. Intravenous injection of cLipG/CuET was conducted every other day from day 0, and intraperitoneal injection of αCTLA-4 started from day 1 and with three times per week. Mice were finally sacrificed at day 21 (Fig. 7A). During the experimental period, the body weight of each mouse maintained stable (Fig. 7C), indicating a good biosafety of the dosage. At day 21, a combination of cLipG/CuET with αCTLA-4 outperformed the single treatment in inhibiting tumor growth and reducing liver weight (Fig. 7B, D).

Hematoxylin and Eosin (H&E) staining consistently offered histopathological evidence that the combination of cLipG/CuET with αCTLA-4 protected the liver tissue in CCA mice more effectively than the monotherapy. Immunohistochemistry (IHC) staining for Ki67 and immunofluorescence staining for TUNEL-positive and CK19 (a CCA marker) indicated that alongside αCTLA-4, cLipG/CuET synergistically inhibited the proliferation promoted the apoptosis of tumor cell in vivo. The anti-tumor effects were further enhanced when cLipG/CuET was combined with αCTLA-4 (Fig. 7E, F). Moreover, it had no significant impact on various biochemical indicators and the morphology of major organs in mice, demonstrating potential therapeutic safety (Fig. S1E, F).

Next, we investigated whether a combination therapy of cLipG/CuET and αCTLA-4 could activate the immune response in CCA mice. The infiltration and activation of antigen-specific $CD8^+$ T cells and $CD4^+$ T cells within the TME are well known for promoting tumor suppression by inducing intercellular immune responses [36]. To further validate the role of cLipG/CuET in amplifying the anti-tumor immunity, T cell infiltration in mouse tumor tissue was detected by flow cytometry. The combination of cLipG/CuET and αCTLA-4 significantly increased the infiltration rate of $CD8^+$ T cells (Fig. 7G) and the proportion of $CD86^+$ M1-TAMs, concomitant with a marked decrease in $CD206^+$ M2-TAMs, compared to other treatment modalities (Fig. 7H, I). Immunofluorescence staining of tumor tissue consistently revealed an increased proportion of M1 cell markers (CD86, red) and a decreased proportion of M2 cell markers (CD206, green) in CCA mice co-treated with cLipG/CuET and

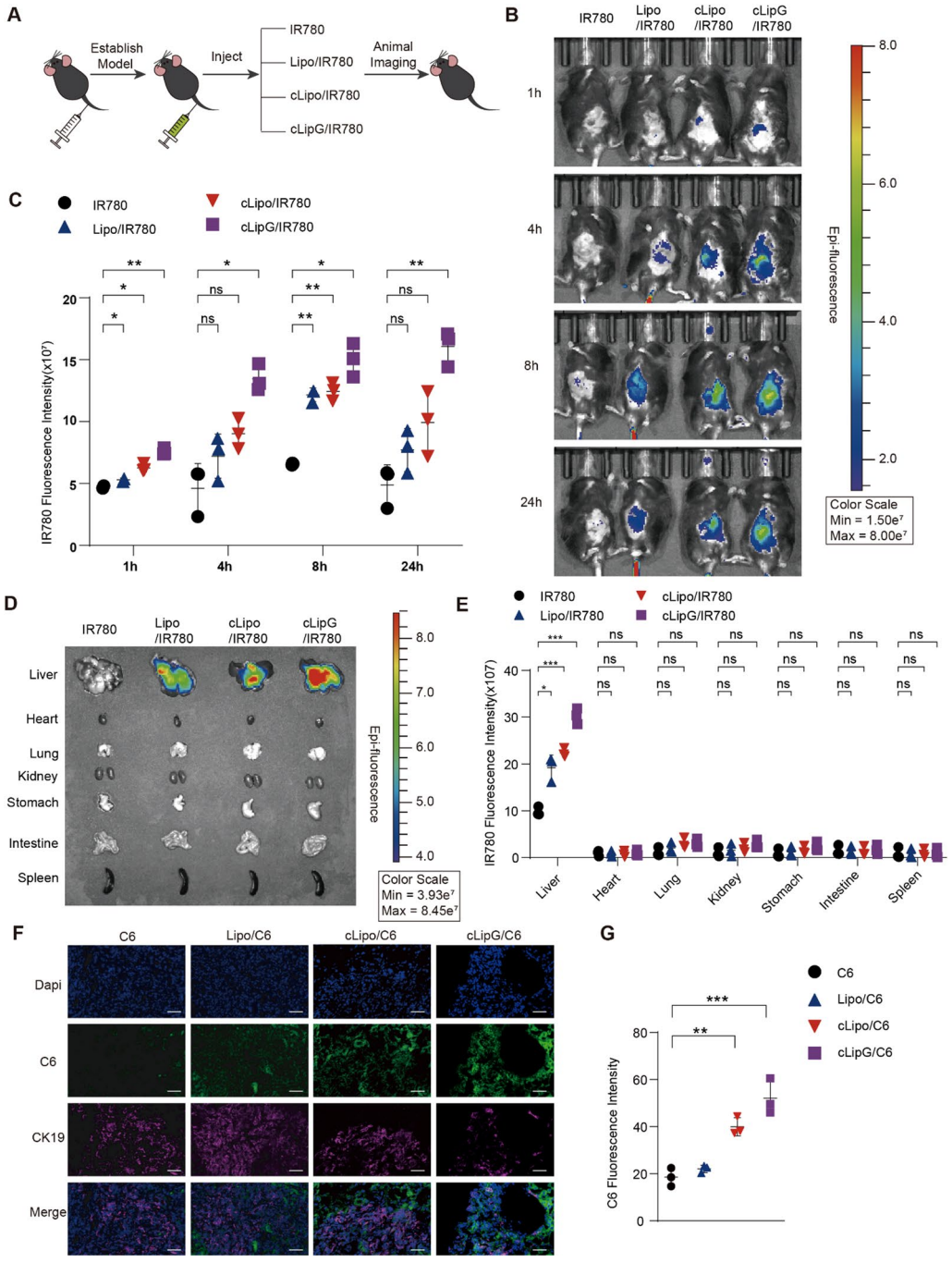

Fig. 6 In vivo Spatial Distribution Pattern of cLipG. **A** A scheme of creating a KRASG12D/P19 plasmid-induced primary CCA mouse model. **B** Representative fluorescence images of the mouse liver acquired at post-injection 1, 4, 8, and 24 h, illustrating the in vivo distribution pattern of cLipG. **C** A semi-quantitative analysis of fluorescence intensity in mouse liver. **D** Ex vivo fluorescence images of IR780 in major organs at post-injection 8 h. **E** A semi-quantitative analysis of fluorescence intensity of IR780 in major organs. **F** Representative images of liver tissue sections stained with CK19 (red) were used to illustrate the distribution pattern at the liver tissue level, scale bar = 100 μm. **G** A semi-quantitative analysis of fluorescence intensity of C6 in mouse liver. One-way ANOVA was conducted (SD, $n = 3$). *$P < 0.05$, **$P < 0.01$, and ***$P < 0.001$

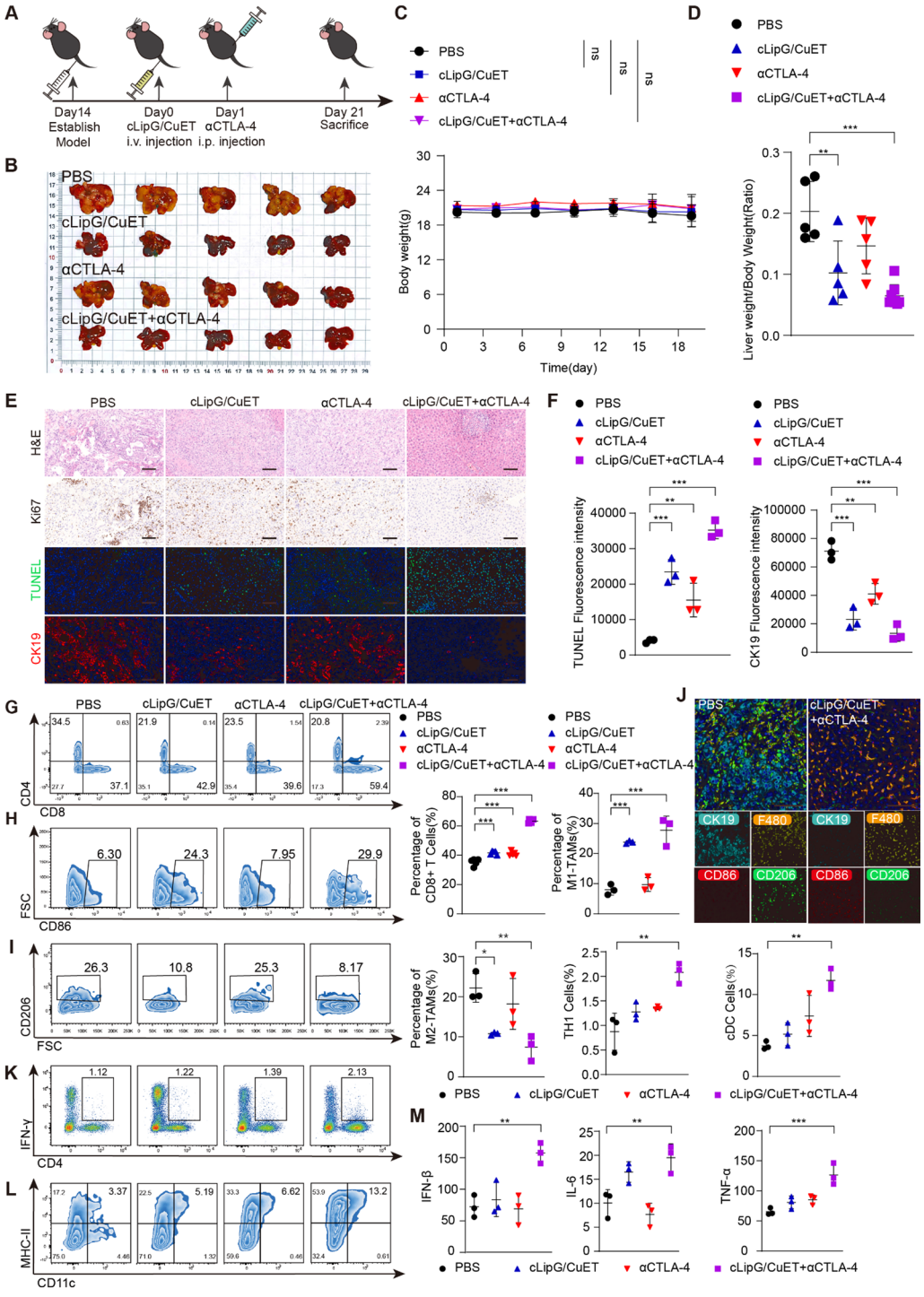

Fig. 7 In vivo Anti-tumor Effects of cLipG/CuET in Combination with αCTLA-4. **A** A scheme of CCA mice with the treatment strategy. **B** Representative liver sections of CCA mice, scale bar = 100 μm. **C** Changes in mouse body weight during the experiment period. **D** Measurement and analysis of the liver-to-body weight ratio. **E** Representative H&E, Ki67, TUNEL, and CK19 staining images of mouse liver sections, scale bar = 100 μm. **F** A semi-quantitative analysis of the fluorescence intensities of TUNEL-positive and CK19-positive areas. **G** Measurements of $CD8^+$ T cells ($CD45^+CD4^+CD8^+$) in tumor samples from treated mice by flow cytometry. **H** Measurements of M1-TAMs ($F4/80^+CD86^+$) in tumor samples from treated mice by flow cytometry. **I** Flow cytometry was employed to analyze M2-TAMs ($F4/80^+CD206^+$) in tumor samples from treated mice by flow cytometry. **J** Fluorescence images of M1-TAMs ($F4/80^+CD86^+$) and M2-TAMs ($F4/80^+CD206^+$) in treated mouse tumor samples. **K** Measurements of cDC cells ($CD11c^+MHC\text{-}II^+$) in tumor samples from treated mice by flow cytometry. **L** Measurements of TH1 cells ($CD4^+IFN\text{-}\gamma^+$) in tumor samples from treated mice by flow cytometry. **M** Detection of IFN-β, IL-6, TNF-α levels released from mouse serum by ELISA. One-way ANOVA was conducted (SD, $n = 3$). $^*P < 0.05$, $^{**}P < 0.01$, and $^{***}P < 0.001$

αCTLA-4 (Fig. 7J). Additionally, we performed flow cytometry analysis on tumor tissues from STING knockout (KO) mice. The results demonstrated no significant differences in the infiltration of M1-TAMs, M2-TAMs, $CD4^+$ T cells, or $CD8^+$ T cells between STING KO mice and PBS-treated controls following drug administration (Fig. S1G, H, I). These findings further validate the consistency of our experimental data.

Moreover, cLipG/CuET + αCTLA-4 combination therapy significantly enhanced the abundances of T helper 1 (TH1) cells (cDCs) (Fig. 7K) and conventional dendritic cells (Fig. 7L), while concurrently elevating the serum levels of key pro-inflammatory cytokines, including IFN-β, IL-6, and TNF-α in treated mice (Fig. 7M). In summary, these findings strongly support the potent protective effect of cLipG/CuET against the progression of ICC by reshaping the immunosuppressive TME.

Discussion

ICC has an incidence that has kept rising annually, and few patients can survive for more than 12 months [37]. Additionally, ICC is marked by a fibrous extracellular matrix and a hypovascular stroma, encompassing both non-immune cells, such as cancer-associated fibroblasts and tumor-associated macrophages, alongside immune cells [3]. These structural characteristics refrain therapeutic agents from reaping optimal outcomes. Research has indicated that the progression of cholangiocarcinoma is linked to mitochondrial dysfunction [38]. Here, we provided a new composite that can target mitochondria to trigger the cGAS/STING pathway, thereby enhancing the innate immune response to improve the outcome of immunotherapy.

Tsvetkov et al. revealed in 2022 that copper toxicity disrupts specific mitochondrial metabolic enzymes, leading to an atypical cell death termed cuproptosis [13]. This mechanism has garnered significant interest within the research community. Our prior studies have demonstrated that copper ions can induce severe mitochondrial damage within cholangiocarcinoma cancer cells [39]. Thus, in this study, we synthesized a novel type of nanoliposome, namely cLipG/CuET, and validated its anti-cancer property against ICC by targeting tumor mitochondria, promoting tumor cell apoptosis, and enhancing immunotherapy through a mitochondrial copper-dependent cell death process. In these nanoliposomes, CTPP successfully reaches the mitochondria of ICC cells, and GA further causes mitochondrial damage by inducing the opening of the MPTP, during which mtDNA fragments are released to activate the cGAS/STING signaling pathway in macrophages, enhance the innate immunity and repolarize TAMs, thereby reversing the immunosuppressive TME. In summary, cLipG/CuET can activate systemic anti-tumor immunity in ICC both in vitro and in vivo. Strikingly, the combination of cLipG/CuET significantly augmented the therapeutic efficacy of αCTLA-4 against ICC, providing a new strategy for implementing immunotherapy.

Materials and methods

Materials

18β-Glycyrrhetinic acid (GA), with a molecular weight (MW) of 470.68Da, Copper (II) Diethyldithiocarbamate (CuET), with a molecular weight (MW) of 360.07Da, Ethyl-3-(3 -dimethylaminopropyl) carbodiimide (EDC), 1-Hydroxy-5-pyrrolidinedione (NHS), octadecylamine (ODA), and (4-Carboxybutyl) triphenylphosphonium bromide (CTPP) were all purchased from Aladdin Reagent Database Inc (Shanghai, China). Dimethyl sulfoxide (DMSO) was purchased from Sigma Reagent. The egg yolk lecithin was purchased from Avida (Shanghai) Pharmaceutical Technology Co., Ltd. (Shanghai, China).

Cell lines and cell culture

HuCCT1 cells (JCRB, Osaka, Japan) were cultured in RPMI-1640 (Invitrogen, Waltham, MA, USA) medium. All cells were maintained under optimal conditions at 37 °C with 5% CO_2 and cultured in a medium supplemented with 10%–20% fetal bovine serum (FBS, Biological Industries, Cromwell, CT, USA), along with antibiotics including 100 U/mL penicillin (Invitrogen) and 100 U/mL streptomycin (Invitrogen).

Synthesis of CTPP-ODA

In this step, 0.100 g of CTPP (carboxylated tripolyphosphate), 0.080 mg of EDC (1-Ethyl-3-(3-dimethylaminopropyl) carbodiimide), 0.100 mg of NHS (N-hydroxysuccinimide) and 0.053 g of ODA (octadecylamine) were mixed with 20 mL of ethanol. The mixture was then left to react overnight under reflux condensation at 60 °C, and then water dialysis for three days using a dialysis bag (Mw = 7 kDa, Shanghai Yuanye Biotechnology Co., LTD.). The resulting solution was centrifuged at 12,000 rpm for 30 min, followed by freeze-drying to obtain CTPP-ODA. The structure of CTPP-ODA was confirmed using a ^1H NMR spectrometer (AC-80, Bruker Biospin, Germany).

Preparation of cLipG/CuET

The nanoagent cLipG/CuET was fabricated utilizing an ethanol injection method. Firstly, a lipid mixture containing lecithin (10 mg), CTPP-ODA (0.5 mg), CuET (0.5 mg), and GA (1.2 mg) was dissolved in 1 ml of anhydrous ethanol and sonicated for 10 min to ensure complete dissolution. Subsequently, the ethanol mixture was injected into 9 ml of rapidly stirring phosphate-buffered saline (PBS) at a constant rate. The solution was then centrifuged at 4000 rpm for 15 min to eliminate

unencapsulated drugs or aggregated particles. The supernatant was sterile-filtered (0.45 μm) for cellular and animal experiments and stored at 4 °C. cLipG, cLipo/CuET, and fluorescently labeled nanoparticles were synthesized using the same methodology.

Physicochemical characterization

After synthesis, the nano reagents were diluted 10 times with either phosphate-buffered saline (PBS) or pure water. Particle size and zeta potential were then measured using dynamic light scattering (DLS) and electrophoretic light scattering (ELS), respectively, with a Zetasizer Nano instrument from Malvern Instruments, Malvern.

In vitro drug release

Using free GA or CuET as control groups, the release of GA or CuET from the lipid-based nanocarriers was investigated in PBS (pH 7.4, 37 °C) using an orbital shaker. The nanomedicines were placed in dialysis bags (Mw = 14 kDa), which were then securely clamped and incubated in 30 mL of PBS within 50 mL centrifuge tubes. At various time intervals, 1 mL of aliquots of the solution within the tubes was collected, replaced with fresh PBS, and quantified using a UV-Vis spectrophotometer at specific wavelengths.

Cellular uptake

The nanoformulation cLipG/C6 was successfully prepared using the ethanol injection method. A lipid mixture containing lecithin (10 mg), CTPP-ODA (0.5 mg), coumarin 6 (C6) (0.5 mg), and GA (1.2 mg) was dissolved in 1 ml of absolute ethanol and sonicated for 10 min to ensure complete dissolution. This ethanolic mixture was then injected at a constant rate into 9 ml of rapidly stirring PBS. The solution was centrifuged at 4000 rpm for 15 min to remove any unencapsulated drug or aggregated particles, and the supernatant was collected. Using the same method but without adding GA or CTPP-ODA, the fluorescence intensity of the obtained liposomes was measured using a microplate reader (Bio-Rad, Harkles, CA, USA).

To evaluate the uptake of C6 by HuCCT1 cells, every 5×10^5 cells were seeded per well in a 6-well plate (Corning, USA). After 24 h of incubation to allow cell attachment, the cells were divided into four groups: C6, Lipo/C6, cLipo/C6, and cLipG/C6 (with a drug concentration of 2 μg/ml). After administration, the cells were incubated for 6 h in the dark, and washed three times with PBS. Fluorescence images were captured using a fluorescence microscope. The fluorescence intensity was quantitatively measured using a BD FACS Canto II flow cytometer (BD Biosciences, CA).

Mitochondrial colocalization

Cells were seeded on coverslips and allowed to adhere, followed by treatment with C6-liposomes for 24 h. Subsequently, the cells were fixed with 4% paraformaldehyde, permeabilized with 0.2% Triton X-100, and blocked with 5% BSA for 30 min. After blocking, the cells were incubated with a primary antibody against TOM20 (ABclonal, Shanghai, China), a mitochondrial marker, at room temperature for 1 h, followed by three rounds of washing with PBS. A red fluorescent dye-conjugated secondary antibody was then applied and incubated for one additional hour. Nuclei were counterstained with DAPI (Beyotime, China). Finally, samples were visualized under a confocal microscope.

Copper uptake

HuCCT1 cells in the logarithmic growth phase were seeded into a 6-well plate (Corning, USA) at a density of 1×10^4 cells per well. After 24 h of adherence, the cells were treated with cLipG, cLipo/CuET, cLipG/CuET at various concentrations, and PBS as a negative control for 24 h. Subsequently, the copper content in the cells or mitochondria isolated using a mitochondria isolation Kit (Beyotime, Shanghai, China) was determined using a kit from Solabio (Beijing, China). The data were then presented in a bar graph using GraphPad Prism 10.

CCK8 viability assay

HuCCT1 cells in the logarithmic growth phase were seeded onto 96-well plates (Corning, USA) at a density of 5×10^3 cells per well. After 24 h, the preparation at varying concentrations was added to the wells, and the cells were further incubated for 24 h in a complete culture medium supplemented with FBS. Culture medium was then replaced with 10 μL of Cell Count Kit-8 (CCK 8, Abbkine Scientific Co., Ltd, Wuhan, China) solution and 90 μL of 1640 basal culture medium. The plates were then incubated for an additional two hours, and the optical density (OD) value of each well was measured at 450 nm using a microplate reader (Bio-Rad, Harkles, CA, USA). Cell viability was calculated using the formula: Cell viability (%) = (ODp - ODb)/(ODc - ODb) × 100%, where ODp represents the OD of the experimental group, ODb is the OD of the cell-free blank group, and ODc is the OD of the group composed of cells treated with blank culture medium. These procedures were repeated in triplicate, and the results were analyzed using GraphPad Prism 10.

Colony formation assay

HuCCT1 cells were seeded into 6-well plates (Corning, USA) at a density of 1×10^3 cells per well. After 24 h, the HuCCT1 cells were treated with different concentrations of cLipG, cLipo/CuET, cLipG/CuET, and PBS (as a negative control) for 24 h. Drug-free complete medium

(containing 10% FBS) was replaced and allowed for an additional eight days of cell culture. Photographs of the colony formation assay were taken, and the number of colonies within the field of view for each treatment group was counted. The data were then presented in a bar graph using GraphPad Prism 10.

Apoptosis assay

HuCCT1 cells were seeded into a 6-well plate (Corning, USA) at a density of 1 × 105 cells per well. Following 24 h of adherence, the cells were treated with liposomes and PBS as a negative control for 24 h. After treatment, cell apoptosis was conducted using the Annexin V-FITC Apoptosis Detection Kit (Beyotime, Shanghai, China). The culture medium was removed, and the cells were washed with PBS, collected after trypsin digestion, and centrifuged. Then, the Annexin V-FITC/PI mixture (comprising of Annexin V (5 μL), Propidium Iodide (PI) (10 μL), and binding buffer (100 μL)) was added, and the cells were incubated in the dark at 37℃ for 15 min. The cells were then filtered and analyzed using a BD FACS Canto II Flow Cytometer (BD Biosciences, CA). The percentage of Annexin V-positive cells (early apoptosis) plus Annexin V/PI double-positive cells (late apoptosis) was calculated as the apoptosis rate. Bar graphs were generated using GraphPad Prism 10.

Western blotting

Tissues and cells were lysed in a complete lysis buffer consisting of RIPA lysis buffer (Biosharp), a mixture of protease and phosphatase inhibitors (Roche Diagnostics GmbH, Mannheim, Germany), and phenylmethylsulfonyl fluoride (PMSF) (Biosharp, Hefei, China), for 30 min on ice. Subsequently, the protein content was quantified using a BCA Protein Assay Kit (Beyotime, Shanghai, China).

Equal amounts of protein were loaded onto 10% or 12% protein gels (TGX Stain-Free FastCast Acrylamide Kit, Bio-Rad Laboratories) and separated by non-reducing SDS-PAGE in Tris-Glycine SDS running buffer. The proteins were transferred onto Immobilon-P PVDF membranes (Millipore) via wet blotting. After incubation with primary antibodies, the bands were detected using a chemiluminescence imaging system (Tanon 5200).

Detection of ATP release

After the adherent cells were challenged with liposomes for 24 h, the ATP concentration in the treated tumor cells or the supernatant was measured according to the method of the ATP Assay Kit (Beyotime, China).

Measurement of mitochondrial membrane potential

After the adherent cells were challenged with liposomes for 24 h, the cells were collected and stained with the JC-1 fluorescent probe using the Enhanced Mitochondrial Membrane Potential Detection Kit (JC-1) (Beyotime, China) for 20 min. Subsequently, images were captured using a fluorescence microscope, and the fluorescence intensity of each sample was quantified via flow cytometry.

MPTP opening assay

After the adherent cells were challenged with liposomes for 24 h, the cells were collected, and the degree of MPTP opening was evaluated using an MPTP Detection Kit (Beyotime, China). The cells were then stained with Calcein-AM and $CoCl_2$ solution for 40 min, and images were captured using a fluorescence microscope.

Intracellular ROS measurement

After the adherent cells were challenged with liposomes for 24 h, the cells were collected and stained with ROS reactive agent (DCFH-DA, 10 μM) using the Reactive Oxygen Species Assay Kit (Beyotime, China). Subsequently, images were captured using a fluorescence microscope, and the fluorescence intensity of each sample was quantified via flow cytometry.

qRT-PCR

RNA was extracted from the treated cells using TRIzol (Invitrogen, America) and dissolved in RNase-free ddH_2O. RNA transcription was repeated using the SuperMix First-Strand Synthesis System (Vazyme, China). The resulting cDNA was subjected to qRT-PCR using ChamQ SYBR Color qPCR Master Mix (Vazyme, China). The levels of obtained mRNAs were analyzed using the 2^-ΔΔCt method for data interpretation.

Quantification of MtDNA in cytosolic extracts

The processed cells were collected and divided into two equal portions. One portion was resuspended in 500 μL of 50 mM HEPES buffer (pH = 7.4) containing 150 mM NaCl and 20 μg/mL digitonin. This suspension was incubated for 15 min to allow selective plasma membrane permeabilization, followed by centrifugation at 17,000 g for 10 min, yielding a cytoplasmic fraction devoid of nuclei, mitochondria, and endoplasmic reticulum. The second portion remained untreated.

DNA was extracted from both groups using the TIANamp Genomic DNA Kit (TIANGEN, China). Subsequently, qPCR was performed on whole-cell extracts and the cytoplasmic fractions using nuclear DNA primers and mtDNA primers. The Ct value obtained for the mtDNA abundance in the whole-cell extracts served as a normalization control for the mtDNA values in the cytoplasmic fractions.

Fluorescence image of MtDNA

Cells were seeded on coverslips and allowed to adhere before being treated with liposomes for 24 h. Subsequently, the cells were fixed with 4% paraformaldehyde, permeabilized with 0.2% Triton X-100, and blocked with 5% BSA for 30 min. After blocking, the cells were incubated with primary antibodies against TOM20 and TFAM at room temperature for 1 h, followed by three rounds of washing with PBS. Secondary antibodies conjugated with green and red fluorescent dyes were added and incubated for one additional hour. Nuclei were counterstained with DAPI (Beyotime, China). Finally, the samples were observed under a confocal microscope.

Activation of cGAS-STING signaling

After the tumor cells adhered to the wall, they were treated with liposomes for 12 h. Subsequently, all treatments were removed, and macrophages were added to the upper chamber for co-incubation for 24 h. The macrophage proteins were then extracted and analyzed using Western blotting. The cell supernatants were collected and subjected to an ELISA kit to detect the production of cGAMP.

Polarization of macrophages

After the tumor cells have adhered to the substrate, they are treated with liposomes for 12 h. Following this, all treatments were removed, and macrophages were added to the upper chamber for co-incubation for an additional 24 h. Subsequently, the macrophages were collected for qRT-PCR analysis. The levels of obtained mRNAs were then quantitatively analyzed using the $2^{-\Delta\Delta Ct}$ method. Additionally, after staining the treated macrophages with antibodies against CD86 and CD206, the polarization of M1 and M2 macrophages was assessed using flow cytometry.

Detection of immunogenic cell death

The HMGB1 promoter fragment was amplified using PCR, and after confirming its correct sequence, it is cloned into the luciferase reporter gene expression vector pGL3. The resulting recombinant plasmid, pGL3-HMGB1P, was then transfected into tumor cells. Following a 24-hour treatment with liposomes, the supernatant was collected and combined with the luciferin, and the bioluminescent signal was immediately detected using a luminometer.

Animal models

Male C57BL/6J mice, weighing 20–22 g and aged 6–7 weeks (GemPharmatech, China), were maintained in a specific pathogen-free (SPF) environment. Each mouse was injected with 25 μg of $KRAS^{G12D}$ and 10 μg of sgP19 plasmids, along with Sleeping Beauty (SB) transposase, via hydrodynamic injection into the tail vein to establish a CCA model.

In vivo distribution of cLipG

After establishing the CCA mouse model, Lipo, cLipo, and cLipG were labeled with IR780. Subsequently, 200 μl of IR780, Lipo/IR780, cLipo/IR780, and cLipG/IR780 solutions were injected into the mouse tail veins, respectively. Using an in vivo imaging system (IVIS Lumina XR, Caliper, USA), the mice were imaged at specific time points to observe the drug distribution based on the fluorescence intensity of IR780. At post-injection 24 h, various organs of the mice were dissected and imaged to visualize drug distribution.

In vivo anti-cancer efficacy

The CCA mouse model was employed to evaluate the anti-cancer activity of cLipG/CuET and its synergistic effect with αCTLA-4. The CCA model mice were randomly divided into four groups: normal control (saline), cLipG/CuET monotherapy, αCTLA-4 monotherapy, and combined treatment with cLipG/CuET and αCTLA-4. For the cLipG/CuET treatment, a tail vein injection was administered every two days, while αCTLA-4 was administered via intraperitoneal injection three times per week. The mice' body weights in each group were recorded throughout the treatment period. After 21 days, the mice were sacrificed, and their liver weights and anti-tumor effects were observed. The excised tumor masses were fixed in 4% paraformaldehyde solution for subsequent H&E staining and IHF staining analysis.

To assess the biosafety of cLipG/CuET, αCTLA-4, and their combination, blood samples and vital organs (lung, kidney, heart, and spleen) were collected from the mice at 21 days after treatment. Serum biochemical analysis was performed to evaluate potential systemic effects. Additionally, the harvested organs were subjected to H&E staining for histological examination to assess tissue damage or abnormalities.

Anti-cancer immune responses

To assess the infiltration of immune cells, we collected livers from mice in different groups at the observation endpoint and cut them into small pieces. Subsequently, these samples were incubated in 2 mL of solution containing 500 μg/mL collagenase IV (Invitrogen), 100 μg/mL hyaluronidase, and 20 U/mL DNase (Macklin) at 37 °C for 30 min. After filtration through a 100-mesh sieve, single-cell suspension was prepared. Next, macrophages were labeled using anti-mouse CD45, CD11b, F4/80, CD86, and CD206 antibodies; $CD8^+$ T cells were labeled with anti-mouse CD3, CD4, and CD8 antibodies; cDC cells were labeled with anti-mouse CD45, CD11b, CD11c, and MHC-II antibodies; TH1 cells were labeled

with anti-mouse CD45, CD3, CD4, and IFN-γ antibodies (BioLegend, USA). Following cell staining, we conducted flow cytometry analysis.

Statistical analysis

Data were presented as mean ± standard deviation (SD) of data from at least three independent experiments. Significant differences between means were assessed via analysis of variance (ANOVA) using GraphPad Prism Version 6. $^{*}P < 0.05$, $^{**}P < 0.01$, and $^{***}P < 0.001$.

Supplementary Information

The online version contains supplementary material available at https://doi.org/10.1186/s12951-025-03689-0.

Supplementary Material 1.

Acknowledgements
Not applicable.

Author contributions
BG, LHW and LW: experiment design and writing. ZY, XL and WL: supervision. BG, LHW and CSJ: doing experiments in vivo and in vitro. BG, LHW and LW: statistical analysis and editing draft. All authors approved the final manuscript.

Funding
Jiangsu provincial key research and development program (BE2023655); National Natural Science Foundation of China (82403645, 82102917, 82473107, 82102984).

Data availability
No datasets were generated or analysed during the current study.

Declarations

Ethics approval and consent to participate
Not applicable.

Consent for publication
All authors agree to publication.

Competing interests
The authors declare no competing interests.

Author details
[1]Department of Gastroenterology, College of Traditional Chinese and Western Medicine, Nanjing Drum Tower Hospital Clinical, Nanjing University of Chinese Medicine, Nanjing 21008, Jiangsu Province, P. R. China
[2]Department of Gastroenterology, Nanjing Drum Tower Hospital, The Affiliated Hospital of Nanjing University Medical School, Nanjing 210008, 21008, Jiangsu Province, P. R. China
[3]Department of Gastroenterology, Nanjing Drum Tower Hospital, Drum Tower Clinical Medical College of China Pharmaceutical University, Nanjing 21008, Jiangsu Province, P. R. China
[4]Department of Pharmacy, Nanjing Drum Tower Hospital, Drum Tower Clinical Medical College of Nanjing Medical University, Nanjing 210008, Jiangsu Province, China

Received: 5 March 2025 / Accepted: 24 August 2025
Published online: 09 October 2025

References

1. Moris D, Palta M, Kim C, Allen PJ, Morse MA, Lidsky ME. Advances in the treatment of intrahepatic cholangiocarcinoma: an overview of the current and future therapeutic landscape for clinicians. Cancer J Clin. 2023;73(2):198–222.
2. Sarcognato S, Sacchi D, Fassan M, Fabris L, Cadamuro M, Zanus G, Cataldo I, Capelli P, Baciorri F, Cacciatore M, et al. Cholangiocarcinoma Pathologica. 2021;113(3):158–69.
3. Sirica AE, Gores GJ. Desmoplastic stroma and cholangiocarcinoma: clinical implications and therapeutic targeting. Hepatology (Baltimore MD). 2014;59(6):2397–402.
4. Chen J, Amoozgar Z, Liu X, Aoki S, Liu Z, Shin SM, Matsui A, Hernandez A, Pu Z, Halvorsen S, et al. Reprogramming the intrahepatic cholangiocarcinoma immune microenvironment by chemotherapy and CTLA-4 Blockade enhances Anti-PD-1 therapy. Cancer Immunol Res. 2024;12(4):400–12.
5. EASL-ILCA Clinical Practice. Guidelines on the management of intrahepatic cholangiocarcinoma. J Hepatol. 2023;79(1):181–208.
6. Jiang M, Chen P, Wang L, Li W, Chen B, Liu Y, Wang H, Zhao S, Ye L, He Y, et al. cGAS-STING, an important pathway in cancer immunotherapy. J Hematol Oncol. 2020;13(1):81.
7. Bakhoum SF, Ngo B, Laughney AM, Cavallo JA, Murphy CJ, Ly P, Shah P, Sriram RK, Watkins TBK, Taunk NK, et al. Chromosomal instability drives metastasis through a cytosolic DNA response. Nature. 2018;553(7689):467–72.
8. Hopfner KP, Hornung V. Molecular mechanisms and cellular functions of cGAS-STING signalling. Nat Rev Mol Cell Biol. 2020;21(9):501–21.
9. Dvorkin S, Cambier S, Volkman HE, Stetson DB. New frontiers in the cGAS-STING intracellular DNA-sensing pathway. Immunity. 2024;57(4):718–30.
10. Ouyang W, Wang S, Yan D, Wu J, Zhang Y, Li W, Hu J, Liu Z. The cGAS-STING pathway-dependent sensing of mitochondrial DNA mediates ocular surface inflammation. Signal Transduct Target Therapy. 2023;8(1):371.
11. Wang Y, Luo J, Alu A, Han X, Wei Y, Wei X. cGAS-STING pathway in cancer biotherapy. Mol Cancer. 2020;19(1):136.
12. Mangalhara KC, Varanasi SK, Johnson MA, Burns MJ, Rojas GR, Esparza Moltó PB, Sainz AG, Tadepalle N, Abbott KL, Mendiratta G, et al. Manipulating mitochondrial electron flow enhances tumor immunogenicity. Sci (New York NY). 2023;381(6664):1316–23.
13. Tsvetkov P, Coy S, Petrova B, Dreishpoon M, Verma A, Abdusamad M, Rossen J, Joesch-Cohen L, Humeidi R, Spangler RD, et al. Copper induces cell death by targeting lipoylated TCA cycle proteins. Sci (New York NY). 2022;375(6586):1254–61.
14. Xie J, Yang Y, Gao Y, He J. Cuproptosis: mechanisms and links with cancers. Mol Cancer. 2023;22(1):46.
15. Bround MJ, Havens JR, York AJ, Sargent MA, Karch J, Molkentin JD. ANT-dependent MPTP underlies necrotic myofiber death in muscular dystrophy. Sci Adv. 2023;9(34):eadi2767.
16. Zhou C, Kuang M, Tao Y, Wang J, Luo Y, Fu Y, Chen Z, Liu Y, Li Z, Wu W, et al. Nynrin preserves hematopoietic stem cell function by inhibiting the mitochondrial permeability transition pore opening. Cell Stem Cell. 2024;31(9):1359–e13751358.
17. Yang M, Zhang M, Liu Q, Xu T, Huang T, Yao D, Wong CW, Liu J, Guan M. 18β-Glycyrrhetinic acid acts through hepatocyte nuclear factor 4 alpha to modulate lipid and carbohydrate metabolism. Pharmacol Res. 2020;157:104840.
18. Wang L, Wang X, Chen F, Song YQ, Nao SC, Chan DS, Wong CY, Wang W, Leung CH. A glycyrrhetinic acid-iridium(III) conjugate as a theranostic NIR probe for hepatocellular carcinoma with mitochondrial-targeting ability. Eur J Med Chem. 2024;264:115995.
19. Fiore C, Salvi M, Palermo M, Sinigaglia G, Armanini D, Toninello A. On the mechanism of mitochondrial permeability transition induction by glycyrrhetinic acid. Biochim Et Biophys Acta (BBA) - Bioenergetics. 2004;1658(3):195–201.
20. Battaglia V, Brunati AM, Fiore C, Rossi CA, Salvi M, Tibaldi E, Palermo M, Armanini D, Toninello A. Glycyrrhetinic acid as inhibitor or amplifier of permeability transition in rat heart mitochondria. Biochim Et Biophys Acta (BBA) - Biomembr. 2008;1778(1):313–23.
21. Biswas S, Dodwadkar NS, Piroyan A, Torchilin VP. Surface conjugation of triphenylphosphonium to target poly(amidoamine) dendrimers to mitochondria. Biomaterials. 2012;33(18):4773–82.
22. Haddad S, Abánades Lázaro I, Fantham M, Mishra A, Silvestre-Albero J, Osterrieth JWM, Kaminski Schierle GS, Kaminski CF, Forgan RS, Fairen-Jimenez D. Design of a functionalized Metal-Organic framework system for enhanced targeted delivery to mitochondria. J Am Chem Soc. 2020;142(14):6661–74.

23. Qian K, Gao S, Jiang Z, Ding Q, Cheng Z. Recent advances in mitochondria-targeting theranostic agents. Exploration. 2024;4(4):20230063.
24. Skrott Z, Mistrik M, Andersen KK, Friis S, Majera D, Gursky J, Ozdian T, Bartkova J, Turi Z, Moudry P, et al. Alcohol-abuse drug Disulfiram targets cancer via p97 Segregase adaptor NPL4. Nature. 2017;552(7684):194–9.
25. Zielonka J, Joseph J, Sikora A, Hardy M, Ouari O, Vasquez-Vivar J, Cheng G, Lopez M, Kalyanaraman B. Mitochondria-Targeted Triphenylphosphonium-Based compounds: syntheses, mechanisms of action, and therapeutic and diagnostic applications. Chem Rev. 2017;117(15):10043–120.
26. Aaron JS, Taylor AB, Chew TL. Image co-localization - co-occurrence versus correlation. J Cell Sci. 2018;131(3):jcs211847.
27. Dunn KW, Kamocka MM, McDonald JH. A practical guide to evaluating colocalization in biological microscopy. Am J Physiol Cell Physiol. 2011;300(4):C723–742.
28. Ianevski A, Giri AK, Aittokallio T. SynergyFinder 2.0: visual analytics of multi-drug combination synergies. Nucleic Acids Res. 2020;48(W1):W488–93.
29. Ianevski A, Giri AK, Aittokallio T. SynergyFinder 3.0: an interactive analysis and consensus interpretation of multi-drug synergies across multiple samples. Nucleic Acids Res. 2022;50(W1):W739–43.
30. Tang D, Kroemer G, Kang R. Targeting Cuproplasia and Cuproptosis in cancer. Nat Reviews Clin Oncol. 2024;21(5):370–88.
31. Bock FJ, Tait SWG. Mitochondria as multifaceted regulators of cell death. Nat Rev Mol Cell Biol. 2020;21(2):85–100.
32. Murphy MP, O'Neill LAJ. A break in mitochondrial endosymbiosis as a basis for inflammatory diseases. Nature. 2024;626(7998):271–9.
33. Wang L, Niu C. IR780-based nanomaterials for cancer imaging and therapy. J Mater Chem B. 2021;9(20):4079–97.
34. Lanng KRB, Lauridsen EL, Jakobsen MR. The balance of STING signaling orchestrates immunity in cancer. Nat Immunol. 2024;25(7):1144–57.
35. Yi M, Li T, Niu M, Mei Q, Zhao B, Chu Q, Dai Z, Wu K. Exploiting innate immunity for cancer immunotherapy. Mol Cancer. 2023;22(1):187.
36. Zeng X, Shapaer T, Tian J, Abudoukelimu A, Zhao Z, Shayimu P, Ma B. Identifying a CD8T cell signature in the tumor microenvironment to forecast gastric cancer outcomes from sequencing data. J Gastrointest Oncol. 2024;15(5):2067–78.
37. Tucek S, Tomasek J, Halámkova J, Kiss I, Andrasina T, Hemmelová B, Adámková-Krákorová D, Vyzula R. Bile duct malignancies. Klinicka Onkologie: Casopis Ceske Slovenske Onkologicke Spolecnosti. 2010;23(4):231–41.
38. Raggi C, Taddei ML, Sacco E, Navari N, Correnti M, Piombanti B, Pastore M, Campani C, Pranzini E, Iorio J, et al. Mitochondrial oxidative metabolism contributes to a cancer stem cell phenotype in cholangiocarcinoma. J Hepatol. 2021;74(6):1373–85.
39. Liu H, Xu L, Zhang Y, Xie Y, Wang L, Zhou Y, Wang Z, Pan Y, Li W, Xu L, et al. Copper increases the sensitivity of cholangiocarcinoma cells to Tripterine by inhibiting TMX2-Mediated unfolded protein reaction activation. Adv Healthc Mater. 2023;12(26):e2300913.

Publisher's note